Numerical analysis of data transfer parameters in transition metals doped multiferroic

M. Tariq [a,b*], R. Ahmed [a, b], S. A. Tahir [a], B.U. Haq [c], F. K. Butt [d], M.W. Majeed [a], A. Hussain [a]

[a] *NRPU Lab, Centre for High Energy Physics, University of the Punjab Quaid-e-Azam Campus, University of the Punjab Lahore, 54590 Pakistan*

[b] *Department of Physics, Faculty of Science, Universiti Teknologi Malaysia, Johor Bahru 81310, Malaysia.*

[c] *Department of Mechanical Engineering, College of Engineering, Prince Mohammad Bin Fahd University, Alkhobar 31952, Saudi Arabia*

[d] *Department of Physics, Division of Science and Technology, University of Education Lahore, 54770, Pakistan*

Bismuth ferrite ($BiFeO_3$, BFO) is a remarkable multiferroic material with excellent magnetoelectric switching properties. This study examines the effect of transition metal (X = Co, Ni, Mn, Ti) doping at the B-site of hexagonal-phase BFO on its spin-polarized electronic, structural, and magnetic properties for data transfer applications, using the generalized gradient approximation plus Hubbard U (GGA+U) method. All doped BFO systems in the hexagonal phase exhibit 100% spin polarization at the Fermi level, except for Ni-doped BFO. In Mn-doped BFO, atoms show an enhanced magnetic moment compared to pure and other doped BFO, indicating a localized impact of Mn on the magnetic structure. The data transfer parameters such as magnetoelectric coefficient and magnetic force per unit area of pure and doped BFO were examined numerically. Mn-doped BFO exhibits an increase in magnetoelectric coefficient (α) and magnetic force per unit area (M_{BFO}) values, with α reaching 2.46×10^{-9} s/m and M_{BFO} increasing to 2.46×10^{-7} V·s/m². Besides this, Co-doped BFO shows moderately high values, with α of 2.30×10^{-9} s/m and a M_{BFO} of 2.30×10^{-7} V·s/m².

(Received March 4, 2025; Accepted October 3, 2025)

Keywords: Magnetic moment, Spin polarization, Magnetoelectric coefficient, Magnetic force

1. Introduction

The growing influence of artificial intelligence (A.I) in computing technology is driving an increasing demand for high speed random access memory (RAM) [1].The existing approach to meeting this demand, which entails minimizing the size of chip and adding the more transistors, will no longer, be useful beyond a certain point. Economic reasons and efficiency constraints are to blame for this, as the costs and challenges of miniaturization continue to rise. Conversely, as the rising A.I sector demands faster and more dependable data processing, the gradation of computing systems will need to improve. This necessitates the development of innovative memory technologies that can keep pace with these evolving requirements[2–4].

The present RAM technology is powered by a linear dielectric capacitor and a complementary metal-oxide semiconductor (CMOS) field-effect transistor in modern computing systems[2]. These components form the backbone of most memory devices today, enabling the storage and retrieval of data. To read and write data, CMOS switching physics solely uses a magnetic field; in this switching process, 90% of energy is squandered, making it highly inefficient [3]. A new switching material and innovative switching mechanism for RAM are required to satisfy this need without consuming energy, which can overcome these limitations and

* Corresponding author: tariq1981@graduate.utm.my
https://doi.org/10.15251/JOR.2025.215.629

provide a more sustainable solution[4]. Therefore, Intel and the University of California, Berkeley have developed an enhanced switching mechanism for the underdevelopment spin RAM technology that is based on the combined state of the material's magnetoelectric and dielectric properties. This innovative approach aims to address the inefficiencies of current memory technologies and pave the way for more energy-efficient and high-performance computing system [5].

Multiferroics can play a key role due to their magneto electric response to develop a fast spintronic RAM technology in future[6]. Their unique combination of switching response allows for the simultaneous control of magnetic and electric properties, making them highly efficient for memory applications[7].Because, the ferromagnetic and ferroelectric are coupled in multiferroics, enabling them to interact and influence each other under the same external conditions. So, they have ability to functioning ferromagnetic and ferroelectric response by applying same electric field, which simplifies the design and operation of spintronic devices[8]. Therefore, the multiferroic materials are currently used in FeRAM and MRAM[5,9]. But , the major drawback of both RAM is that they require a significant amount of current (5 μA) to reset [10], which raises energy more energy consumption and reduces the effectiveness. This issue can be resolved with the help of a single phase multiferroic, whose ferroelectric and ferromagnetic response can be controlled with help of electric field or magnetic field[11]. This adaptability allows for more efficient switching mechanism with reduced energy requirements. Therefore, the only device material that can attain optimally low switching energy is a single-phase multiferroic, making it a promising candidate for next-generation memory technologies[12].

An appropriate single-phase multiferroic with fascinating magnetoelectric behavior for RAM is bismuth ferrite $BiFeO_3$ (BFO) [13]. This material stands out due to its unique ability to transport information through the switchable ferromagnetic and ferroelectric response. Unfortunately, the BFO material still faces challenges due to its unbalanced ability to flip between magnotoelectric and ferroelectric states. This imbalance limits its efficiency, as it exhibits significantly stronger ferroelectric switching responsiveness compared to its weak ferromagnetic switching behavior under the same electric field. This discrepancy may be attributed to its low magnetic moment of 0.1 $\mu_{B,}$ high ferroelectric polarization ranging from 90 to 95 μC/cm^2, and a colossal dielectric constant value of 1000 [14],[15], [16]. Additionally, oxygen vacancies influence volume magnetism by creating localized charges, though excessive vacancies can lead to increased leakage current and reduced magnetic stability. These properties contribute to its weak magnetoelectric coupling and strong ferroelectric switching, which hinder its overall performance in practical applications[17–19].

In its pure form, BFO exhibits a weak magnetic moment, typically around 0.1 μ_B, due to its antiferromagnetic (AFM) nature. This weak magnetic moment is a result of the G-type antiferromagnetic ordering, where the magnetic moments of iron (Fe) ions align in opposite directions, canceling out most of the net magnetization.So, In the hexagonal phase of BFO, the magnetism is primarily governed by the antiferromagnetic interactions between of Fe ions. These interactions are relatively weak, resulting in a low magnetic force and limited magnetoelectric coupling. These weak magnetic properties of BFO addressed in different studies[20][21] with B-site dopant elements[22][23].For instance, P. Iyyappa Ragan et al. [24] conducted DFT calculations and found that Ni increases magnetic moment in BFO due to double exchange magnetic interactions. In its tetragonal structure, the magnetic moment of Fe was observed to be 4.13 μ_B in DFT studies [25], primarily arising from the Fe-3*d* states [26]. S. Jakub et al. [27] reported Fe(3.73 μ_B) magnetic moment in rhombohedral structure using GGA+U calculations, which aligns closely with the same value of magnetic moment predicted by Geneste et al. [28]. They observed that enhancement in bond length (Fe-O) can be caused an increased the magnetic moment of Fe to 3.5 μ_B as the charge decreases. Kadim et al. [29] obtained a relatively higher magnetic moment of 4.02 μ_B for Fe in g-type AFM BFO. Despite advancements in enhancing the magnetic moment of BFO, the volume magnetization, magnetoelectric coupling coefficient, volume magnetism and magnetic force per unit area of BFO in hexagonal phase remains unexplored in DFT studies. While the magnetic properties of BFO in the cubic phase has been previously investigated[7] in our work, but its hexagonal phase remains unexplored. In this study,

we explore the volume magnetization, magnetoelectric coupling coefficient, and magnetic force per unit area of both pure and doped BFO in the hexagonal phase.

The magnetic switching properties of BFO can be enhanced through doping with transition metals, which disrupt the antiferromagnetic order and introduce ferromagnetic (FM) interactions. For instance, doping with cobalt (Co) or manganese (Mn) alters the spin structure and introduces additional magnetic interactions, significantly increasing the magnetic moment. Dopants also modify magnetoelectric coupling coefficient and magnetic force per unit area by altering the crystal structure and interactions between magnetic ions, often reducing antiferromagnetic interactions and increasing net magnetization.

In this study, DFT calculations were performed to investigate the spin-polarized electronic, magnetic, and structural properties of doped BFO in hexagonal phase. Notable changes were observed following doping with Ni, Mn, Ti, and Co, which are detailed in the subsequent sections. The structure of the paper is as follows: section 2 presents the computational methodology, while Section 3 examines the structural properties, magnetic moment, and volume magnetization. Finally, Section 4 provides a summary of all the findings.

2. Computational details

The study employs the CASTEP code within the plane-wave pseudo potential approach. The exchange correlation functional is treated using the Generalized Gradient Approximation (CGA-PBE) [30]. The investigation focuses on the structural, spin-polarized electronic, magnetic, and structural properties of pure and (Ti, Mn, Co, Ni) doped $BiFeO_3$ (BFO) in its hexagonal phase. The hexagonal lattice parameters are $a = b = 5.576$ Å and $c = 13.858837$ Å. The atomic positions are Bi: (0.00, 0.00, 0.00), Fe: (0.00, 0.00, 0.22046), and O: (0.44506, 0.01789, 0.95152). The convergence criteria include an electromagnetic energy threshold of 10^{-4} eV, cut-off energy of 489 eV, and residual force minimization below 0.03 eV/ Å. CASTEP settings for co-doped BFO simulations are set to medium quality. Brillouin-zone sampling is performed using a 4x4x4 *K*-point grid (32 irreducible *K*-points). The self-consistent field (SCF) calculations achieve an accuracy of $1x10^{-6}$ eV. The primary focus is on the volume magnetism, magnetoelectric coupling coefficient, and magnetic force per unit area capabilities of pure and doped BFO in hexagonal. A 2x2x1 supercell of BFO is used in the hexagonal structure as shown in Fig.1. The CGA+U method was utilized to incorporate correlation effects in the transition metal oxide, with an effective Hubbard U parameter (U-J) of 4 eV applied to the Fe atom [31].

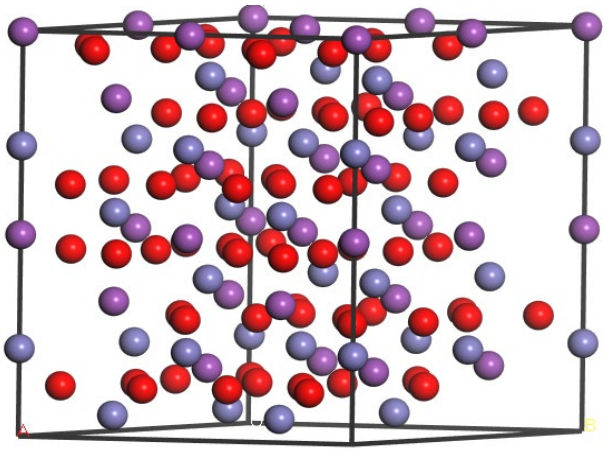

Fig. 1. Presentation of a three-dimensional 2x2x1 super cell structure, comprising pure BFO in its hexagonal phase. The color scheme denotes oxygen (red), bismuth (purple), and iron (dark gray) atoms.

3. Results and discussion

3.1. Structural properties

The Lattice constants, average bond lengths, and unit cells volume of pure and doped BFO in the hexagonal phase exhibit notable variations upon doping. For pure BFO, the lattice parameters are $a = b = 5.57$ Å and $c = 13.86$ Å, with an average X-O bond length of 2.11 Å and a unit cell volume of 373.84 Å^3.Our calculated lattice parameters are in good agreement with reported lattice parameters of BFO in hexagonal phase [24]. Upon Co doping, the lattice constants slightly decrease to $a = b = 5.54$ Å, while c remains unchanged at 13.86 Å, resulting in a reduced bond length of 2.02 Å and a volume of 373.80 Å^3. In contrast, Ni doping decreases the lattice parameters to $a = b = 5.56$ Å and c =13.86 Å, with an average bond length of 2.07 Å and a volume of 373.83 Å^3. Similarly, Mn doping a decrease the structure, yielding $a = b = 5.56$ Å, $c = 13.86$ Å, and bond length of 2.05 Å, with a volume of 373.83 Å^3. The lattice parameters of BFO might decrease by changing the Fe^{+4} to Fe^{+3} cations in presences of Mn impurity atom, reducing oxygen vacancies in the BFO structure and consequently decreasing the lattice parameters[32]. The most significant expansion is observed in Ti-doped BFO, where the lattice parameters reach $a = b = 5.70$ Å and $c = 13.89$ Å, with the longest bond length of 2.19 Å and a volume of 373.86 Å^3. The increment in lattice paramters after introducing the Ti impurity atoms is attributed to mighty reactive response of Ti with localized charge and high effective mass[33].

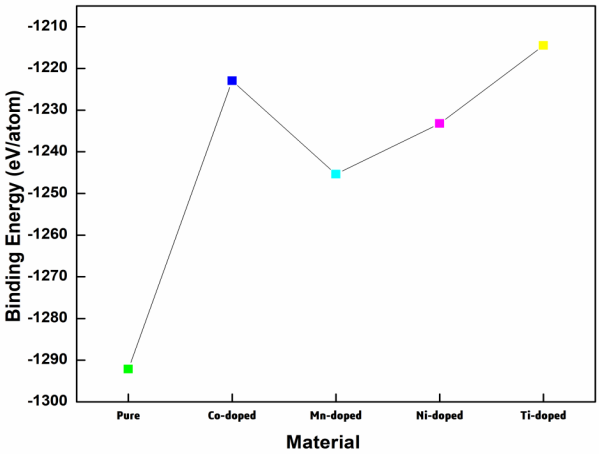

Fig. 2. The calculated binding energy of pure and doped BFO.

Binding energy of pure and doped BFO has been calculated from pseudopotential energy file and represented in Fig.2. The more negative values indicate that stronger atomic interactions and enhanced stability. Fig.2 reveals that pure BFO has the more negative binding energy, leading to more stable structure. Among doped systems, Mn-doped BFO shows the high negative binding energy (-1245.38 eV/atom), making it the most stable structure of BFO in hexagonal phase. The high negative binding energy of Mn doped BFO can be attributed to Mn incorporation strengthens Fe-O-Mn, super-exchange interactions. Besides this, moderate negative binding energy is appeared in Ni doped BFO due to close ionic radii to Fe^{+3}, leading to less distortion in structure compared to Co and Ti atoms. The significant structural weakening is appeared in Co doped BFO due to charge imbalance by $C0^{+2}/Co^{+3}$ substitutions, inducing oxygen vacancies. The least stable structure in doped hexagonal phase of BFO is Ti doped material. The less negative value of Ti doped BFO indicate the presences of Ti^{+4} ions , whose ionic radius are much smaller than Fe^{+3} , leading major distortion in BFO structure[34]. Overall, the stability ranking from most to least stable is: pure BFO> Mn-doped BFO > Ni-doped BFO > Co-doped BFO > Ti-doped BFO.

3.2. Spin-polarized electronic properties

The spin-polarized band gaps and overall electronic nature of pure and doped BFO show significant variations as shown in Fig.3. Pure BFO has a spin-up band gap of 1.56 eV and a spin-down band gap of 1.05 eV, classifying it as a semiconductor[35] with zero spin polarization at the Fermi level. All doped BFO showed half metallic nature except Ni doped BFO as shown in Fig. 3 with 100 % spin polarization for data transfer.

Ti-doped BFO has a zero band gap in the spin-up state and a .053 eV gap in the spin-down state, confirming its half metallic nature due to ionic nature Ti. In Mn-doped BFO, the spin-up channel has a zero band gap, but a gap on 1.1 eV appears slightly above the Fermi level, while the spin-down band gap is 0.63 eV, making it half metallic. The fall in band band gap in Mn doped BFO can be attributed to reduced lattice constant and bond length. The inverse relation between interatomic distance and lattice constant is already reported[36].So increased binding forces requires more energy to break the tight binding of valance electrons and atoms.

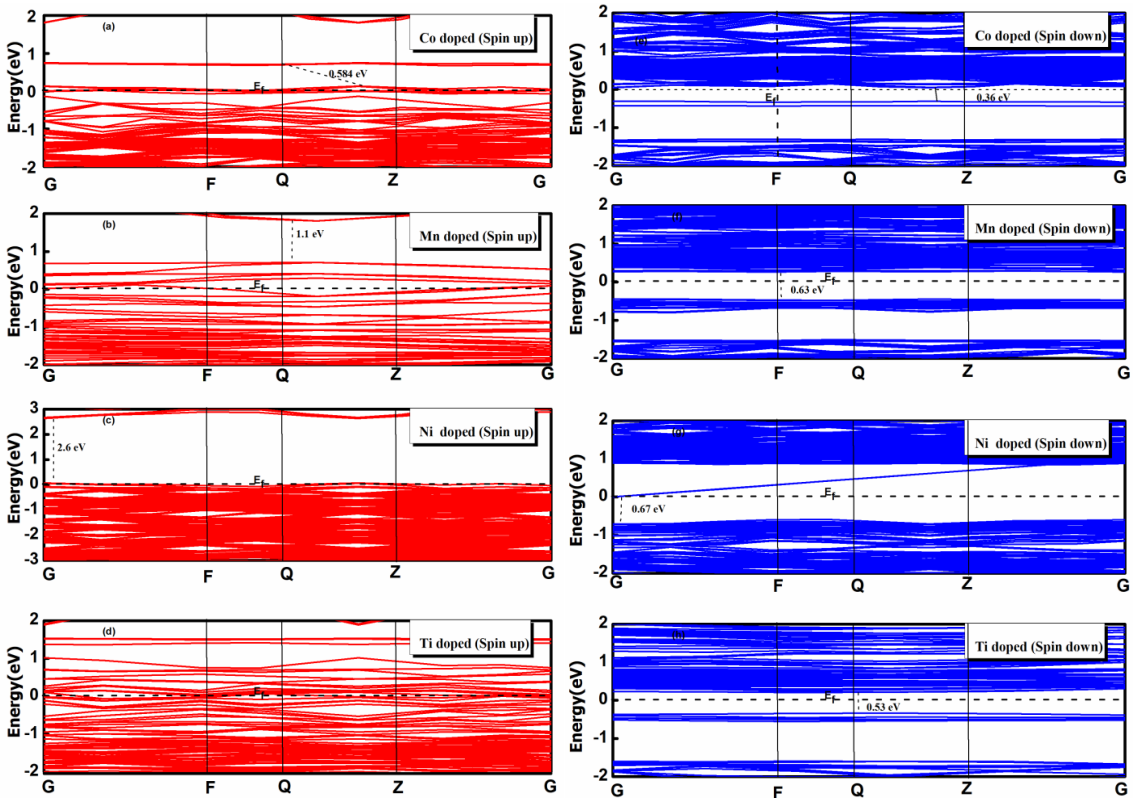

Fig. 3. The calculated spin-polarized band gap of pure and doped $BiFeO_3$ in hexagonal phase.

Consequently, it reduced the band gap. Furthermore, Ni doping results in a spin-up band gap of 2.6 eV and a spin-down band gap of 0.67 eV, maintaining its semiconducting nature. This reduction in band gap can be attributed to enhanced band width of valance band due to occupied Ni (3*d*) splitting states [37]. Furthermore, Co-doped BFO exhibits reduce band gaps of 0.584 eV for spin-up and 0.36 eV for spin-down, indicating a shift toward half metallic behavior. The reduced band gap is attributed to different charge and energy states of both atoms Co and Fe. The band gap minimization in Co-doped BFO is already reported in literature due to smaller oxidation reduction potential of Fe atom, leading to oxidize Fe^{+2} to Fe^{+3} states[38].

3.3. Magnetic moment

The magnetic moment analysis reveals significant variations in Fe atoms upon doping in BFO. In Mn-doped BFO, 5 out of 24 Fe atoms exhibit an enhanced magnetic moment compared to

pure BFO, indicating a localized impact of Mn on the magnetic structure. In contrast, Ni doping induces a more widespread effect, with 20 out of 24 Fe atoms showing an increased magnetic moment, suggesting a stronger influence on the overall magnetization. Co doping results in 8 out of 24 Fe atoms displaying a higher magnetic moment than in pure BFO, indicating a moderate effect on spin polarization. However, Ti doping leads to a reduction in the magnetic moment across all 24 Fe atoms, highlighting its weakening impact on the magnetic properties of BFO. These variations demonstrate how different dopants selectively alter the magnetic interactions within the material.

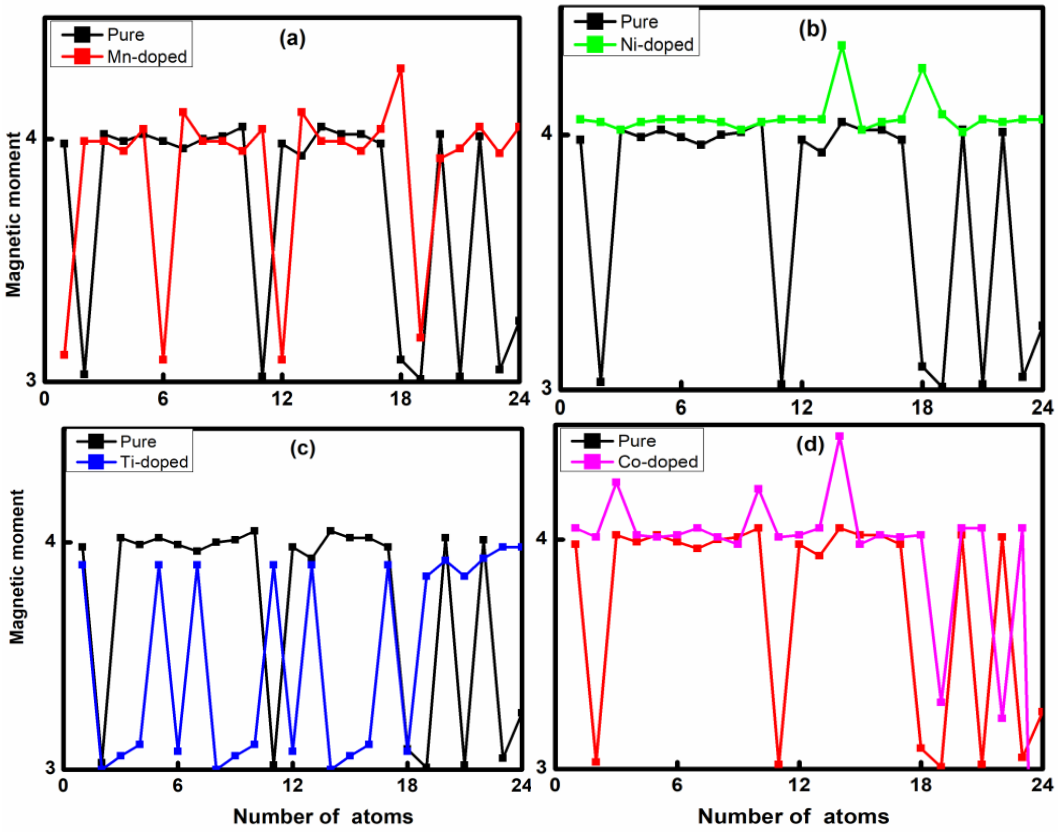

Fig. 4. Comparative analysis of magnet moment of 24 Fe atoms in pure and doped systems with (a)Mn (b)Ni ,(c)Ti and (d)Co atoms.

The magnetic moment analysis reveals a consistent pattern across different doped BFO systems. In Mn-, Ni-, and Co-doped BFO, all 24 atoms exhibit the same magnetic moment as observed in Ti-doped BFO when compared to pure BFO, with only a single atom showing a slight deviation. However, in Ti-doped BFO, 23 atoms maintain the same magnetic moment as in the pure system, while one atom displays an increase magnetic moment. This suggests that Ti-doping introduces a minimal but localized impact on the magnetic structure, whereas other dopants do not significantly alter the overall magnetic distribution in the system.

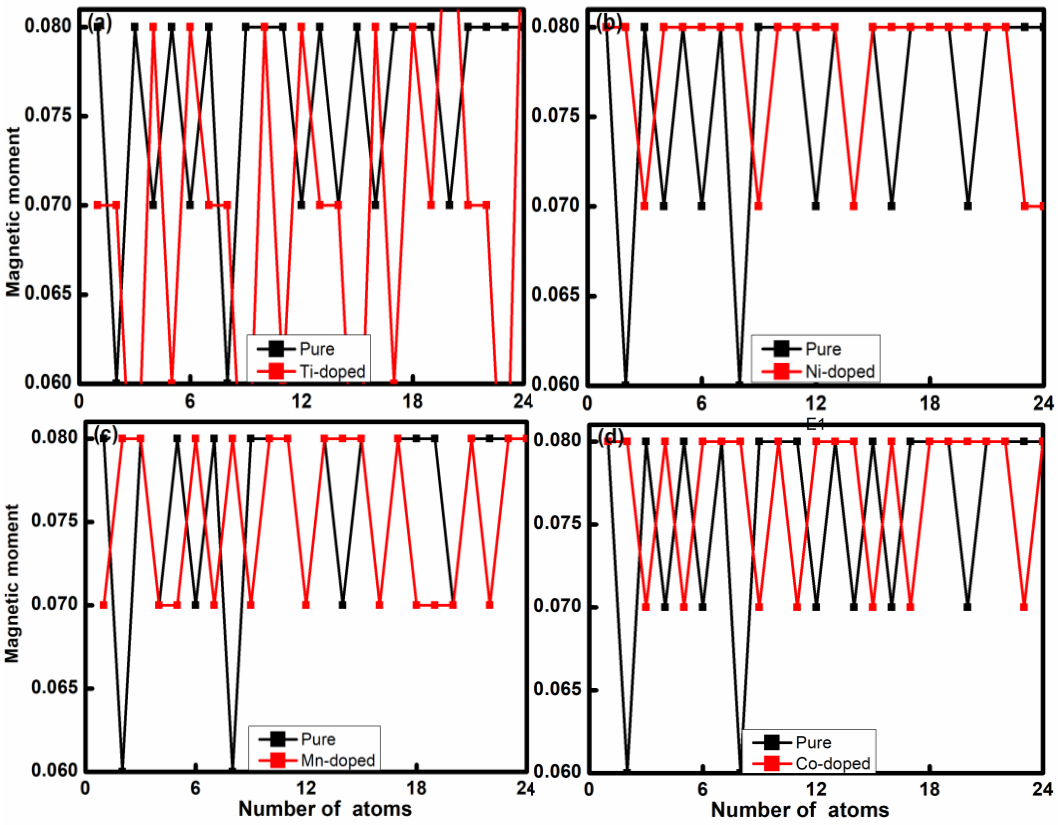

Fig. 5. Comparative analysis of magnet moment of 24 Bi atoms in pure and doped systems with (a)Ti (b)Ni, (c) Mn and (d)Co atoms.

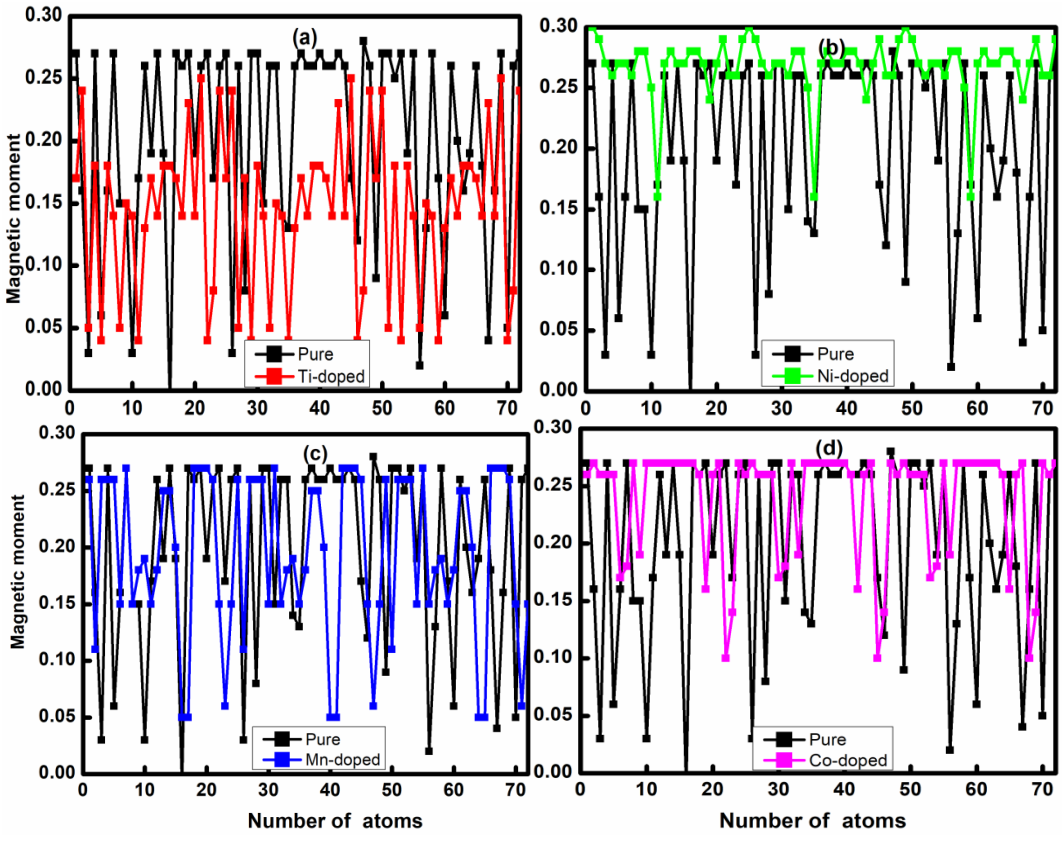

Fig. 6. Comparative analysis of magnet moment of 72 O atoms in pure and doped systems with (a)Ti (b)Ni, (c)Mn and (d)Co atoms.

The impact of doping on the magnetic moments of oxygen atoms in BFO varies depending on the dopant type. In Mn-doped BFO, only two oxygen atoms retain the same magnetic moment as in pure BFO, suggesting a localized influence of Mn on the oxygen sublattice, in Ni-doping BFO, this effect extends to 34 oxygen atoms, indicating a broader but still selective impact on the magnetic structure. In contrast, Co doping does not alter the magnetic moment of any oxygen atoms, as all 72 atoms maintain the same values as in the pure system. However, Ti-doping reduces the magnetic moment across all 72 oxygen atoms, demonstrating its overall weakening effect on the magnetic intersection with in the material. These variations highlight the differing roles of dopants in modifying the spin environment of oxygen atoms in BFO.

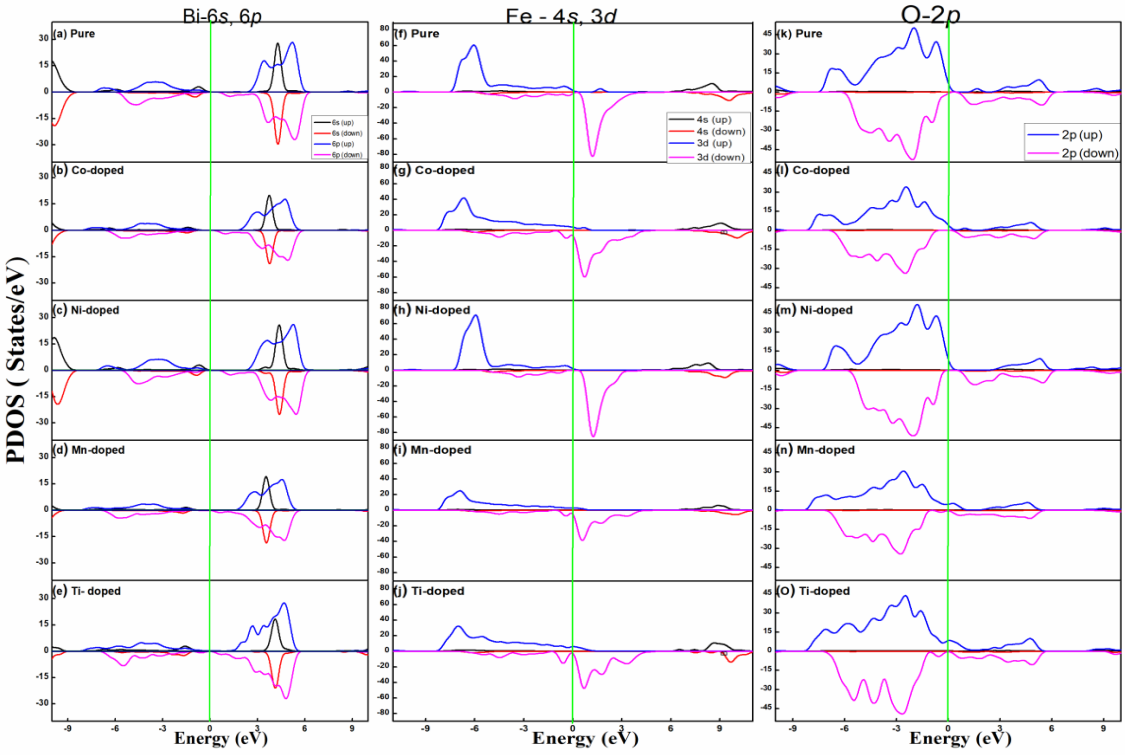

Fig. 7. The calculated spin-polarized partial density of states (PDOS) of Bi (a, b, c, d, e), Fe (f, g, h, i, j), and O (k, l, m, n, o).

The partial density of states (PDOS) analysis provides insights into the relationship between electronic states and magnetic moments in doped BFO. In pure BFO, the spin-up channel exhibits a peak of 70 states/eV at 6 eV in the conduction band, while the spin-down channel shows a similar peak at 2.5 eV in the valence band. This symmetric distribution of states indicates a balanced spin configuration, contribution to a stable magnetic moment. Upon Co doping, the spin-up channel experiences a reduced peak of 40 states/eV at 6 eV, while the spin-down channel shifts significantly, with a peak of 60 states/eV at 0.1 eV in the valance band intersecting the Fermi level. This strong spin asymmetry enhances the net magnetic moment by favoring spin polarization. In Ni-doped BFO the spin-up channel exhibits a peak of 75 states/eV at 5 eV in the conduction band, while the spin down channel shows a peak of 70 states/eV at 0.9 eV in the valance band the relatively small difference between spin-up and spin-down significant redistribution of states, with the spin-up channel showing a peak of 25 states / eV at 6 eV, indicating a shift of states toward the Fermi level. Meanwhile, the spin-down channel displays a peak of 40 states / eV at 0.1 eV, intersecting the Fermi level, further increasing spin imbalance and enhancing the magnetic moment. These variations in PDOS demonstrate how different dopants influence the spin polarization and magnetic properties of BFO, with Co and Mn doping leading to the most pronounced effects.

3.4. Data transfer parameters

The data transfer parameters, such as volume magnetism (M), magnetoelectric coupling coefficient (α), and the magnetic force per unit area exerted by pure and doped BFO on a nano-magnet to store data in spintronic RAM, were examined [39] [5]. The volume magnetism (M) [40] has been calculated with equation as given below

$$M = \frac{M_t\,(\mathrm{Am^2})}{\Omega_o(\mathrm{m^3})} \times 0.927 \times 10^{-24} \quad (1)$$

Here M_t and Ω_o represent the total magnetic moment and volume of unit cell in hexagonal structure.

The total magnetic moment of each atom in BFO has been calculated and presented in Table 1. The total magnetic moment of each atom in different $BiFeO_3$ (BFO) compositions varies depending on the dopant type in pure BFO, the total magnetic moment is 4.83 μ_B, with contribution form Bi (0.07 μ_B), Fe (4.00 μ_B) and oxygen (0.76 μ_B), resulting in a volume magnetism of 1.20 MA/cm.

Table 1. The calculated magnetic moment of Bi, Fe, O and total magnetic of pure and doped BFO with volume magnetism.

Material	Bi (μ_B)	Fe (μ_B)	3O (μ_B)	Total (μ_B)	M (A/m)
Pure	0.7	4.00	0.76	4.83	12.94
Mn-doped BFO	0.7	4.52	0.93	5.52	14.77
Ni-doped BFO	0.7	4.03	0.45	4.55	12.18
Co-doped BFO	0.7	4.13	0.98	5.18	13.80
Ti-doped BFO	0.7	3.21	0.21	3.49	9.27

Upon Ni doping, the Fe moment slightly increases to 4.03 μ_B, but the oxygen contribution decreases to 0.45 μ_B, leading to a reduced total moment of 4.55 μ_B and an increased volume magnetism of 12.18 A/m. In Mn-doped BFO, the Fe moment rises significantly to 4.52 μ_B while the oxygen contribution reaches 0.93 μ_B, increasing the total moment to 5.52 μ_B, with a corresponding volume magnetism of 14.77 M/m. Co doping leads to a total moment of 5.18 μ_B, with Fe and oxygen moments of 4.13 μ_B and 0.98 μ_B, respectively, yielding a volume magnetism of MA/cm. Conversely, Ti doping significantly reduces the Fe moment to 3.21 μ_B and the oxygen contribution 0.21 μ_B, resulting in the lowest total magnetism moment of 3.49 μ_B and a volume magnetism of 0.865 MA/cm.

These variations highlight the impact of dopants on the magnetic properties of BFO, affecting both the total moment and volume magnetism is a systematic manner. Mn doped BFO shown the maximum increment in magnetic moment and volume magnetism .This may be attributed to the enhancement in exchange interactions of Fe atoms, which disturbs the cycloid spin structure of BFO[35].

Furthermore magnetoelectric coupling coefficient (α) is calculated as[41]

$$\alpha_E = \frac{\mu_o M}{E} \quad (2)$$

The magnetic force per unit area exerted by BFO material (M_{BFO}) to transfer the data in spintronic RAM is given as[42]

$$M_{BFO} = \alpha \frac{V_{ISHE}}{l} \quad (3)$$

Here l = 9 mm shows the thickness of BFO with spin Hall Effect voltage 0.9 V [39] [5]. The calculated magnetoelectric coefficient (α) and the magnetic force per unit area (M_{BFO}) exerted by pure and doped BFO on a nano-magnet for data storage in spintronic RAM have been illustrated in Table 2. For pure BFO, the magnetoelectric coefficient is found to be 2.16 $\times 10^{-9}$ s/m, while the corresponding magnetic force per unit area is 2.16 $\times 10^{-7}$ V.s/m². Similarly, M. Bibes et al.[43] examined multiferroic BFO, and found α between 10^{-9} and 10^{-8} s/m.

Table 2. The calculated magneto electric coefficient and magnetic force per unit area exerted by pure and doped BFO on nano-magnet to store the data in spintronic RAM.

Material	α (sec/m)	M_{BFO} (V.sec/m^2)
Pure	2.16×10^{-9}	2.16×10^{-7}
Mn-doped BFO	2.46×10^{-9}	2.46×10^{-7}
Ni-doped BFO	2.03×10^{-9}	2.03×10^{-7}
Co-doped BFO	2.30×10^{-9}	2.30×10^{-7}
Ti-doped BFO	1.54×10^{-9}	1.54×10^{-7}

The magnetoelectric coefficient (α) slightly decreases to 2.03 × 10^{-9} s/m, while M_{BFO} also reduces to 2.03 × 10^{-7} V·s/m² in Ni-doped BFO. J. H. Lee et al. [44] found perovskite oxide-based magnetic tunnel junctions (MTJs) to exhibit α and M_{BFO} identical values in the range of 10^{-9} to 10^{-8} s/m and 10^{-7} V·s/m², respectively. Conversely, Mn-doped BFO exhibits an increase in these values, with α reaching 2.46×10^{-9} s/m and M_{BFO} increasing to 2.46 $\times 10^{-7}$ V·s/m². So, Mn doping enhances the exchange interactions among iron (Fe) atoms, which plays a crucial role in modifying the material's magnetoelectric behavior. The cycloid spin structure of BFO in hexagonal phase is disturbed due to Mn doping, leading to alterations that can result in the development of a high magnetic moment. Additionally, Mn, having a different number of *d*-electrons compared to Fe, influences the overall magnetization, contributing to its increase. Spatial and magneto-crystalline anisotropy also play a role in improving the magnetic moment. Furthermore, Mn doping helps unlock spin blockage in BFO, leading to a net magnetic moment that aligns with reported values[45]. Consequently, these changes collectively demonstrate the significant impact of Mn doping on the spin structure and magnetoelectric improvement in BFO. Besides this, Co-doped BFO shows moderately high values, with a magnetoelectric coefficient of 2.30 $\times 10^{-9}$ s/m and a magnetic force per unit area of 2.30 $\times 10^{-7}$ V·s/m². However, Ti-doped BFO demonstrates the lowest values among the considered dopants, with α at 1.54 $\times 10^{-9}$ s/m and M_{BFO} at 1.54 $\times 10^{-7}$ V·s/m².

4. Conclusion

The study employs the CASTEP code within the plane-wave pseudopotential approach. The effect of transition metals (X = Co, Ni, Mn, Ti) doped at the B-site of BFO in hexagonal phase, on spin-polarized electronic, structural, and magnetic properties for data transfer parameters was examined using generalized gradient approximation plus Hubbard U (GGA+U. All doped BFO systems in the hexagonal phase exhibit 100% spin polarization at the Fermi level, except for Ni-doped BFO. In Mn-doped BFO, 5 out of 24 Fe atoms exhibit an enhanced magnetic moment compared to pure BFO, indicating a localized impact of Mn on the magnetic structure. In contrast, Ni doping induces a more widespread effect, with 20 out of 24 Fe atoms showing an increased

magnetic moment, suggesting a stronger influence on the overall magnetization. Upon Mn doping, the Fe moment slightly increases to 4.03 μ_B, leading to increased volume magnetism of 1.28 MA/cm. In Ni-doped BFO, the Fe moment rises significantly to 4.52 μ_B while the oxygen contribution reaches 0.93 μ_B, increasing the total moment to 5.52 μ_B, with a corresponding volume magnetism of 1.21 MA/cm. Co doping leads to a total moment of 5.18 μ_B, with Fe and oxygen moments of 4.13 μ_B and 0.98 μ_B, respectively, yielding a volume magnetism of 1.13 MA/cm. Conversely, Ti doping significantly reduces the Fe moment to 3.21 μ_B and the oxygen contribution 0.21 μ_B, resulting in the lowest total magnetism moment of 3.49 μ_B and a volume magnetism of 0.865 MA/cm. In Mn-doped BFO, atoms show an enhanced magnetic moment compared to pure and other doped BFO, indicating a localized impact of Mn on the magnetic structure. The data transfer parameters such as magnetoelectric coefficient and magnetic force per unit area of pure and doped BFO were examined numerically. Mn-doped BFO exhibits an increase in magnetoelectric coefficient (α) and magnetic force per unit area (M_{BFO}) values, with α reaching 2.46×10^{-9} s/m and M_{BFO} increasing to 2.46×10^{-7} V·s/m². Besides this, Co-doped BFO shows moderately high values, with α of 2.30×10^{-9} s/m and a M_{BFO} of 2.30×10^{-7} V·s/m².

Acknowledgment

This research was supported by the Higher Education Commission of Pakistan through the National Research Programme for Universities-NRPU with Research Project No. 20-16683/NRPU/R&D/HEC/2021.

References

[1] A. Sebastian, M. Le Gallo, G. W. Burr, S. Kim, M. Brightsky, E. Eleftheriou, Journal of Applied Physics 124 (2018); https://doi.org/10.1063/1.5042413

[2] S. Manipatruni, D. E. Nikonov, C. Lin, T. A. Gosavi, H. Liu, B. Prasad, Y. Huang, E. Bonturim, R. Ramesh, I. A. Young, Nature 565, 35-42 (2019); https://doi.org/10.1038/s41586-018-0770-2

[3] S. Manipatruni, D. E. Nikonov, R. Ramesh, H. Li, I. A. Young, ArXiv (2017), 1-60.

[4] Y. Pan, J. Zhou, Physical Review Applied 10, 1 (2020); https://doi.org/10.1103/PhysRevApplied.14.014024

[5] S. Manipatruni, D. E. Nikonov, I. A. Young, Nature Physics 14, 338-43 (2018); https://doi.org/10.1038/s41567-018-0101-4

[6] M. Tariq, A. Shaari, K. Chaudhary, A. Jalil, F. D. Ismail, R. Ahmed, S. A. Ehsan, Materials Science and Engineering B 300, 117070 (2024); https://doi.org/10.1016/j.mseb.2023.117070

[7] M. Tariq, A. Shaari, K. Chaudhary, R. Ahmed, M. A. Jalil, F. D. Ismail, Physica B: Condensed Matter 652, 414650 (2023); https://doi.org/10.1016/j.physb.2023.414650

[8] S. Hait, S. Ghose, K. Mandal, Journal of Alloys and Compounds 822, 153614 (2020); https://doi.org/10.1016/j.jallcom.2019.153614

[9] E. S. Leland, P. R. Kinget, I. Kymissis, D. Steingart, S. R. Sanders, S. O'Brien, IEEE Nanotechnology Magazine 13, 8-17 (2019); https://doi.org/10.1109/MNANO.2018.2881331

[10] N. V. Srihari, K. B. Vinayakumar, K. K. Nagaraja, Coatings 10, 1-19 (2020); https://doi.org/10.3390/coatings10121221

[11] X. Liang, A. Matyushov, P. Hayes, V. Schell, C. Dong, H. Chen, Y. He, A. Will-Cole, E. Quandt, P. Martins, J. McCord, M. Medarde, S. Lanceros-Mendez, S. Van Dijken, N. X. Sun, J. Sort, IEEE Transactions on Magnetics 57, 1-110 (2021); https://doi.org/10.1109/TMAG.2021.3086635

[12] R. S. Fishman, Physica B:.physb.2017.09.103; https://doi.org/10.1055/s-0043-116983

[13] R. K. Kotnala, J. Shah, Ferrite Materials: Nano to Spintronics Regime, vol. 23, Elsevier

(2015); https://doi.org/10.1016/B978-0-444-63528-0.00004-8

[14] Y. Chu, L. W. Martin, M. B. Holcomb, R. Ramesh, Materials Today 10, 16-23 (2007) Condensed Matter 536, 115-17 (2018); https://doi.org/10.1016/S1369-7021(07)70241-9

[15] J. B. Neaton, C. Ederer, U. V. Waghmare, N. A. Spaldin, K. M. Rabe, Physical Review B 71, 014113 (2005); https://doi.org/10.1103/PhysRevB.71.014113

[16] S. Mohammadi, H. Shokrollahi, M. H. Basiri, Journal of Magnetism and Magnetic Materials 375, 38-42 (2015); https://doi.org/10.1016/j.jmmm.2014.09.050

[17] S. L. Shang, G. Sheng, Y. Wang, L. Q. Chen, Z. K. Liu, Physical Review B 80, 052102 (2009); https://doi.org/10.1103/PhysRevB.80.052102

[18] E. Heifets, E. A. Kotomin, A. A. Bagaturyants, J. Maier, Physical Chemistry Chemical Physics 19, 3738-55 (2017); https://doi.org/10.1039/C6CP07986E

[19] F. Ahmad, I. Naz, J. K. Jang, J. Y. Rhee, Journal of the Korean Physical Society 70, 394-400 (2017); https://doi.org/10.3938/jkps.70.394

[20] A. Fernando, A. Perej, E. Gil-gonz, M. Kowalczyk, E. S. Pedro, P. Luis, Low Temperature Magnetic Transition of BiFeO3 Ceramics Sintered by Electric Field-Assisted Methods: Flash and Spark Plasma Sintering (2023).

[21] B. Ramachandran, M. S. R. Rao, Applied Physics Letters 142505, 2007-10 (2014); https://doi.org/10.1063/1.3242411

[22] Y. Wang, Z. Guo, Q. Jia, J. Dong, J. Zhang, D. Chen, Journal of Alloys and Compounds 786, 385-93 (2019); https://doi.org/10.1016/j.jallcom.2019.01.369

[23] G. Le Bras, D. Colson, A. Forget, N. Genand-Riondet, R. Tourbot, P. Bonville, Physical Review B 80, 1-9 (2009).

[24] P. I. Rajan, S. Mahalakshmi, S. Chandra, Computational Materials Science 130, 84-90 (2017); https://doi.org/10.1016/j.commatsci.2016.12.034

[25] K. Wang, N. Si, Y. Zhang, F. Zhang, A. Guo, W. Jiang, Vacuum 165, 105-12 (2019); https://doi.org/10.1016/j.vacuum.2019.04.009

[26] N. A. Spaldin, R. Ramesh, Nature Materials 18, 203-12 (2019); https://doi.org/10.1038/s41563-018-0275-2

[27] J. Kaczkowski, M. Pugaczowa-Michalska, I. Płowaś-Korus, Physical Chemistry Chemical Physics 23, 8571-84 (2021); https://doi.org/10.1039/D0CP06157C

[28] G. Geneste, C. Paillard, B. Dkhil, Physical Review B 99, 024104 (2019); https://doi.org/10.1103/PhysRevB.99.024104

[29] G. Kadim, R. Masrour, A. Jabar, International Journal of Energy Research 45, 9961-9 (2021); https://doi.org/10.1002/er.6490

[30] M. Tariq, A. Shaari, K. Chaudhary, R. Ahmed, M. A. Jalil, F. D. Ismail, Physica B: Condensed Matter 650, 414489 (2023); https://doi.org/10.1016/j.physb.2022.414489

[31] Q. Y. Rong, L. L. Wang, W. Z. Xiao, L. Xu, Physica B: Condensed Matter 457, 1-4 (2015); https://doi.org/10.1016/j.physb.2014.08.028

[32] Q. Tan, Q. Wang, Y. Liu, Materials 11, 985 (2018); https://doi.org/10.3390/ma11060985

[33] J. Gebhardt, A. M. Rappe, Physical Review B 98, 125202 (2018); https://doi.org/10.1103/PhysRevB.98.125202

[34] D. C. Ghosh, R. Biswas, Theoretical Calculation of Absolute Radii of Atoms and Ions. Part 1. The Atomic Radii (2002), 87-113; https://doi.org/10.3390/i3020087

[35] M. Tariq, A. Shaari, K. Chaudhary, R. Ahmed, F. D. Ismail, Physica B: Condensed Matter 691, 416326 (2024); https://doi.org/10.1016/j.physb.2024.416326

[36] R. Dalven, Physical Review B 8, 6033-4 (1973); https://doi.org/10.1103/PhysRevB.8.6033

[37] Y. Liu, Z. Wang, D. Chang, Q. Sun, M. Chao, Y. Jia, Computational Materials Science 113, 198-202 (2016); https://doi.org/10.1016/j.commatsci.2015.11.041

[38] C. Quan, Y. Han, N. Gao, W. Mao, J. Zhang, J. Yang, X. Li, W. Huang, Ceramics

International 42, 537-44 (2016); https://doi.org/10.1016/j.ceramint.2015.08.142

[39] S. Manipatruni, D. E. Nikonov, C. Lin, B. Prasad, Y. Huang, A. R. Damodaran, Z. Chen, R. Ramesh, I. A. Young, Science Advances 4, 1-9 (2018); https://doi.org/10.1126/sciadv.aat4229

[40] R. K. Kotnala, J. Shah, Ferrite Materials: Nano to Spintronics Regime, vol. 23, Elsevier (2015); https://doi.org/10.1016/B978-0-444-63528-0.00004-8

[41] M. M. Vopson, Critical Reviews in Solid State and Materials Sciences 40, 1-43 (2015); https://doi.org/10.1080/10408436.2014.992584

[42] S. Manipatruni, D. E. Nikonov, R. Ramesh, H. Li, I. A. Young, Spin-Orbit Logic with Magnetoelectric Switching: A Multi-Generation Scalable Charge Mediated Nonvolatile Spintronic Logic (2017), 1-60.

[43] M. Bibes, Nature Materials 7, 7-8 (2008); https://doi.org/10.1038/nmat2189

[44] M. G. Blamire, M. Ali, C. W. Leung, C. H. Marrows, B. J. Hickey, Physical Review Letters 98, 1-4 (2007); https://doi.org/10.1103/PhysRevLett.98.217202

[45] S. E. Musavi Ghahfarokhi, M. R. Larki, I. Kazeminezhad, Vacuum 173, 109143 (2020); https://doi.org/10.1016/j.vacuum.2019.109143